Optics Communications 281 (2008) 4899–4905

Contents lists available at ScienceDirect

Optics Communications

journal homepage: www.elsevier.com/locate/optcom

Numerical approach for designing a Bragg grating acousto-optic modulator using the finite element and the transfer matrix methods

R.A. Oliveira *, P.T. Neves Jr., J.T. Pereira, A.A.P. Pohl

Federal University of Technology – Paraná – UTFPR, Av. Sete de Setembro, 3165, Curitiba – PR, CEP 80230-901, Brazil

ARTICLE INFO

Article history:
Received 19 April 2008
Received in revised form 18 June 2008
Accepted 18 June 2008

Keywords:
Fiber Bragg grating
Acousto-optic modulator
Finite element method
Transfer matrix method

ABSTRACT

The finite element and transfer matrix methods are applied in the design of a Bragg grating acousto-optic modulator. For simulation purposes, the device is taken as a single structure, composed of the silica horn and the fiber Bragg grating. The approach allows the strain field to be completely characterized along the whole structure and leads to a better understanding of the influence of the horn dimensions on the design and performance of the modulator. Results obtained using the two methods show an excellent agreement with experimental data in similar structures of the same dimensions.

1. Introduction

The acousto-optic effect has been successfully used since the early 80s in the design and construction of a variety of optical fiber devices such as frequency shifters [1], tapers and couplers [2], filters [3,4] and modulators [5]. Particularly, acoustic waves can be employed to modulate the spectrum [6] and switch the wavelength [7] of fiber Bragg gratings (FBG). For instance, when an acoustic extensional wave of high frequency propagating along the fiber is coupled into a FBG inscribed in its core it causes the formation of a standing mechanical wave, creating compression and rarefaction zones within the grating planes. The resulting periodic strain modulation causes additional bands to appear on both sides of the grating reflection spectrum. This phenomenon, known as superlattice modulation, was first reported in [8]. The modulation of the FBG can also be understood as a periodic chirp induced by the acoustic wave and has found application in tunable reflectors [9] and in Q-switched DFB lasers [10].

The study of the acousto-optic (AO) mechanism requires the understanding of acoustic waves propagating in fibers, which are usually modeled as thin, uniform rods [11]. Several models have been developed to compute the strain caused in the fiber by the application of a load. However, if the structure under analysis presents an arbitrary cross-sectional shape one needs to adopt an accurate numerical method, such as the finite element method (FEM) [12,13]. This method has been applied in several areas and particularly to study the behavior of strain in polarization maintaining fibers [14]. At the same time one needs to consider how the resulting strain impacts the power exchange of the electromagnetic modes propagating in the fiber. Usually the effect is studied with the help of the coupled-mode theory [15], in which the strain contribution is incorporated into an effective change of the dielectric permittivity of the fiber through a longitudinal strain distribution function [16], which should be known beforehand. The coupled-mode theory can also be applied for obtaining information on the spectral behavior of fiber gratings [17,18]. For cases where the grating is chirped one can use the transfer matrix method (TMM) for arriving at the reflection and transmission spectra resulting from the mode coupling, whereby the grating is divided into discrete uniform sections. The resulting spectrum is then obtained by multiplying an array of matrices, each of which is associated with these sections.

In this work, we apply the FEM and TMM for designing a fiber Bragg grating AO modulator (FBG-AOM). In practice, the modulator is made of several parts put together using different materials and processing techniques. However, for design purposes, we consider the modulator as made of a single block as seen in Fig. 1. As the structure presents a variable shape along the longitudinal axis, the FEM is best suited to study the problem with the required accuracy. The FEM approach allows the strain field caused by the acoustic wave to be completely characterized along the structure while the TMM is used to obtain the spectrum of the corresponding chirped grating. A similar theoretical approach is used to calculate the spectral response of a fiber Bragg grating sensor embedded in a host material system [14].

The real AO modulator is made of a length of silica fiber, in which the grating is inscribed. The region where the grating is

* Corresponding author. Tel.: +55 41 3310 4695.
E-mail address: roberson_assis@cpgei.cefetpr.br (R.A. Oliveira).

0030-4018/$ - see front matter © 2008 Elsevier B.V. All rights reserved.
doi:10.1016/j.optcom.2008.06.047

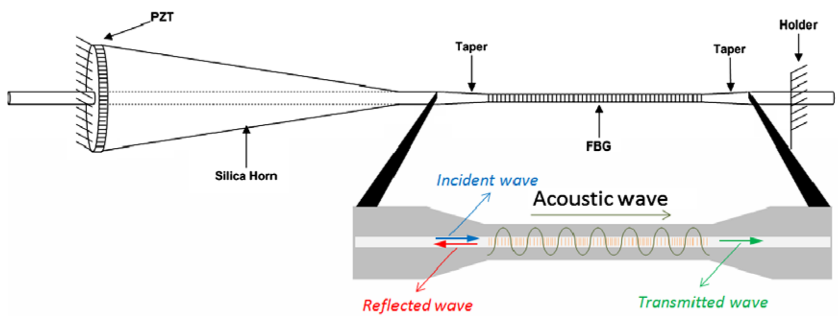

Fig. 1. Schematic diagram of the BG-AOM under excitation of an acoustic wave.

located presents a diameter smaller than the fiber out diameter in order to enhance the acousto-optic interaction excited by the acoustic wave. The length of fiber with the grating is then inserted into a silica horn, which has a piezoelectric (PZT) element in the form of a disc attached to its larger diameter (see Fig. 1). The functioning of the device has been explained and experimentally demonstrated in [4,19–21]. The acoustic wave is generated by the oscillating PZT and is coupled to the optical fiber by means of the silica acoustic horn [6,22].

2. Methodology

The methodology applied to simulate the behavior of the device consists of two steps. First the strain field in the whole structure (horn, taper and FBG) is obtained by using the FEM. Further, the calculated strain field is used in the TMM algorithm to obtain the reflected FBG spectrum.

2.1. The finite element method

The finite element method was introduced in the late 1950s in the aircraft industry [13]. The main advantages of the method are: its widespread acceptance in the scientific and industrial community, the capability of modeling complex geometries, the consistent treatment of differential-type boundary conditions, and the possibility to be programmed in a flexible and general purpose format. Standard finite element approximations are based upon the Galerkin formulation of the weighted residuals method. In this approach the difference between the finite element solution and the analytical solution is minimized with respect to the approximation functions [12].

Fig. 2 shows the 1-D discretization of the FBG-AOM, whose main parts are shown in Fig. 1. The structure is composed of N one-dimensional elements of length $\Delta z = L_D/N$ separated by nodes, where L_D is the total length of the FBG-AOM. Each element is associated with a value that represents the area of the structure at that section.

The differential equation of motion that represents the acoustic wave propagation in the structure is given by

$$E\frac{\partial}{\partial z}\left(A(z)\frac{\partial u(z,t)}{\partial z}\right) - \rho A(z)\frac{\partial^2 u(z,t)}{\partial t^2} = 0, \tag{1}$$

where u is the axial displacement, which is dependent on the position z and on the time t, and $\partial u/\partial z$ is the longitudinal strain ε. The term $A(z)$ accounts for the variable size of the structure along the z axis. E is the Young modulus and ρ is the density, assumed to be 72.5 GPa and 2200 kg/m^3 for the silica, respectively. In the analysis the damping of the acoustical wave in the structure is neglected.

The initial and boundary conditions are given by

$$\begin{cases} \left[AE\frac{du}{dz}\right]_{z=0} = P(t) = P_{DC} + P_0\exp(j\omega t) \\ \qquad u(L_D, t) = 0 \end{cases}. \tag{2}$$

The external excitation $P(t)$ is applied as the combination of a constant load (P_{DC}) and a harmonic load of frequency ω and amplitude P_0 generated by the PZT.

A classical linear basis approach for the finite elements is used in this work. After the one-dimensional discretization, the final matrix form of the problem is given by

$$\mathbf{M}\ddot{\mathbf{u}} + \mathbf{K}\mathbf{u} = \mathbf{P}. \tag{3}$$

In this expression, **M** and **K** are the mass and stiffness matrices of the structure, obtained by the superposition of the mass and stiffness matrix of each element, which are given by

$$[M_{ij}^e] = \frac{\rho A^e \Delta z}{2}\begin{bmatrix} 1 & 0 \\ 0 & 1 \end{bmatrix} \tag{4}$$

and

$$[K_{ij}^e] = \frac{A^e E}{\Delta z}\begin{bmatrix} 1 & -1 \\ -1 & 1 \end{bmatrix}, \tag{5}$$

respectively. The superscript e represents an element with particular properties. Furthermore, **u** and $\ddot{\mathbf{u}}$ in (3) represent the nodal displacement and acceleration vectors, respectively. The vector **P** is the nodal generalized force and has a null value, except for the first component, associated with the node at $z = 0$. For the simulation, the applied load is assumed as being a concentrated point load at the base (larger diameter) of the silica horn. Considering the excita-

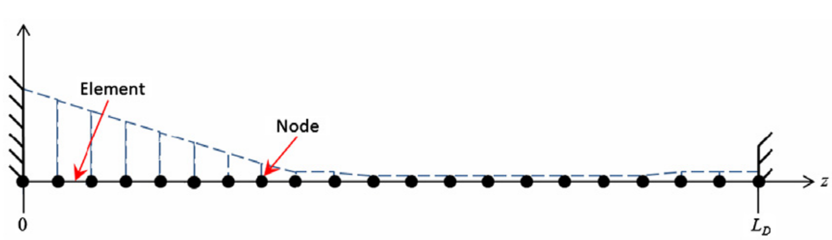

Fig. 2. Discretization of the FBG-AOM in linear elements. Each element has a characteristic function area.

tion in the form of $\mathbf{P} = \mathbf{P}_{DC} + \mathbf{P}_0 \exp(j\omega t)$ and assuming that the system behaves linearly, the solution of the problem can be found solving the following equations:

$$\mathbf{M}\ddot{\mathbf{u}}_{DC} + \mathbf{K}\mathbf{u}_{DC} = \mathbf{P}_{DC}, \tag{6}$$
$$\mathbf{M}\ddot{\mathbf{u}}_t + \mathbf{K}\mathbf{u}_t = \mathbf{P}_0 \exp(j\omega t). \tag{7}$$

Eq. (6) represents the contribution of the component $\mathbf{P}_{DC}$, which is understood as a static pre-tension applied to the structure before the onset of the acoustical wave. Therefore, the acceleration is null and (6) can be reduced to

$$\mathbf{u}_{DC} = \mathbf{K}^{-1}\mathbf{P}_{DC}. \tag{8}$$

On the other hand, since the time dependent load generated by the piezoelectric is harmonic, the solution for (7) has the form $\mathbf{u}_t = \mathbf{u}_0 \exp(j\omega t)$. This way, (7) will be reduced to

$$(-\omega^2\mathbf{M} + \mathbf{K})\mathbf{u}_0 = \mathbf{P}_0. \tag{9}$$

Note that $\mathbf{u}_0$, the displacement vector solution, is highly dependent on the amplitude $\mathbf{P}_0$ and frequency ω of the acoustic excitation. Thus, the complete solution will be given by

$$\mathbf{u} = \mathbf{u}_{DC} + \mathbf{u}_0. \tag{10}$$

Once the displacement field is obtained, the strain field in each one of the finite elements can be found by differentiation, as

$$\varepsilon^e = \frac{u^{e+1} - u^e}{\Delta z}. \tag{11}$$

In this case, as the finite element is linear, u^{e+1} and u^e are the displacements in the local nodes $e + 1$ and e, respectively.

2.2. The transfer matrix method

Bragg gratings are fabricated exposing the core of an optical fiber to ultra-violet radiation. The result for an uniform grating is an effective refraction index (n_{eff}) perturbation in the core described by

$$\Delta n_{\text{eff}}(z) = \Delta\bar{n}_{\text{eff}}(z)\left\{1 + v\cos\left[\frac{2\pi}{\Lambda}\right]\right\}, \tag{12}$$

where $\Delta\bar{n}_{\text{eff}}$ is the average change of the effective refraction index (also called modulation index), v is the fringe visibility (assumed unitary in this paper) and Λ is the grating nominal pitch.

As the grating imposes a dielectric perturbation to the waveguide, it forces coupling between the propagating modes. The theory of coupled-modes [15,16] is a useful and well proven tool for describing this behavior. A set of coupled first-order differential equations given by

$$\frac{dR}{dz} = j\hat{\sigma}R(z) + j\kappa S(z), \tag{13}$$
$$\frac{dS}{dz} = -j\hat{\sigma}S(z) - j\kappa^* R(z), \tag{14}$$

is used to describe the propagation, where $R(z)$ and $S(z)$ represent the propagating and counter-propagating modes, respectively. In these equations $\hat{\sigma}$ represents the general "dc" self-coupling coefficient, which is written as a sum of two parameters:

$$\hat{\sigma} = \delta + \sigma. \tag{15}$$

The term δ, called detuning, is defined as

$$\delta = 2\pi n_{\text{eff}}\left(\frac{1}{\lambda} - \frac{1}{\lambda_D}\right), \tag{16}$$

where $\lambda_D \equiv 2n_{\text{eff}}\Lambda$ is the "design wavelength" for a Bragg scattering within an infinitesimal variation of the effective index ($\Delta n_{\text{eff}} \to 0$), i.e., a grating that is infinitely weak. The parameter σ and κ are given by the equations below,

$$\sigma = \frac{2\pi}{\lambda}\Delta\bar{n}_{\text{eff}}, \tag{17}$$
$$\kappa = \frac{\pi}{\lambda}\Delta\bar{n}_{\text{eff}}. \tag{18}$$

This description represents the situation for a uniform grating, where the average refraction index change is constant. However, the onset of the acoustical wave causes a chirp in the grating, making its pitch nonuniform. In this case, the reflection and transmission spectra from the two-mode coupling can be calculated by considering a piecewise approach, whereby the grating is divided into discrete uniform sections that are individually represented by a matrix. The solution is found by multiplying the matrices associated with each one of the sections. The characteristic equation is solved by making the matrix determinant equal to zero and the resulting polynomial enables the eigenvalues to be found.

The grating of length L can be treated as a quadripole, as shown in Fig. 3. R and S represent the co-propagating and counter-propagating modes, respectively. For convenience, the amplitude $R(0)$ of the incident wave is normalized, in such a way that the maximum value is equal to unit at the origin ($z = 0$).

Splitting the grating in M uniform sections and defining R_i and S_i as amplitudes of the fields across the section i, the propagation through the section is described by the equation

$$\begin{bmatrix} R_i \\ S_i \end{bmatrix} = \mathbf{F}_i^B \begin{bmatrix} R_{i-1} \\ S_{i-1} \end{bmatrix}, \tag{19}$$

where $\mathbf{F}_i^B$ is a 2×2 matrix given by

$$\mathbf{F}_i^B = \begin{bmatrix} \cosh(\gamma_B\Delta z) - j\frac{\hat{\sigma}}{\gamma_B}\sinh(\gamma_B\Delta z) & -j\frac{\kappa}{\gamma_B}\sinh(\gamma_B\Delta z) \\ j\frac{\kappa}{\gamma_B}\sinh(\gamma_B\Delta z) & \cosh(\gamma_B\Delta z) + j\frac{\hat{\sigma}}{\gamma_B}\sinh(\gamma_B\Delta z) \end{bmatrix}, \tag{20}$$

where Δz is the length of the ith uniform section and $\gamma_B \equiv \sqrt{\kappa^2 - \hat{\sigma}^2}$. The coefficients $\hat{\sigma}$ and κ have local values at the ith section.

Since the matrices for each section are known, the application of the boundary conditions, $R(0) = 1$ for $z \leqslant 0$ and $S(L) = 0$ for $z \geqslant L$, allows the final equation to be described as

$$\begin{bmatrix} R(0) \\ S(0) \end{bmatrix} = \mathbf{F}^B \begin{bmatrix} R(L) \\ S(L) \end{bmatrix} \Rightarrow \begin{bmatrix} 1 \\ S(0) \end{bmatrix} = \mathbf{F}^B \begin{bmatrix} R(L) \\ 0 \end{bmatrix}, \tag{21}$$

where

$$\mathbf{F}^B = \prod_{i=1}^{M} \mathbf{F}_i^B. \tag{22}$$

Writing $\mathbf{F}_i^B$ in the form of

$$F_i^B = \begin{bmatrix} f_{11} & f_{12} \\ f_{21} & f_{22} \end{bmatrix} \tag{23}$$

and substituting it in (21), the result is

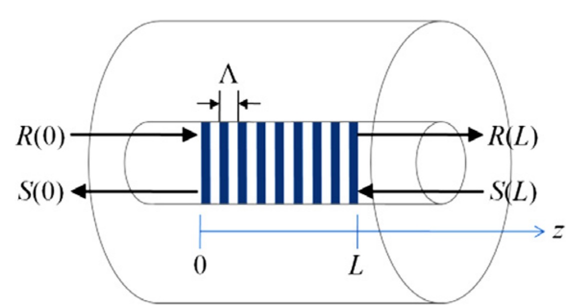

Fig. 3. Bragg grating in the core of an optical fiber.

$$\begin{bmatrix} 1 \\ S(0) \end{bmatrix} = \begin{bmatrix} f_{11}R(L) \\ f_{21}R(L) \end{bmatrix}. \tag{24}$$

From (24) one concludes that $R(L) = \frac{1}{f_{11}}$. Therefore, the reflected amplitude for each wavelength can be found as

$$\zeta(\lambda) = \frac{S(0)}{R(0)} = \frac{S(0)}{1} = \frac{f_{21}}{f_{11}}, \tag{25}$$

and the reflected power will be given by $r(\lambda) = |\zeta(\lambda)|^2$.

Similarly, the transmitted amplitude will be given by

$$\tau(\lambda) = \frac{R(L)}{R(0)} = \frac{R(L)}{1} = \frac{1}{f_{11}}, \tag{26}$$

and the transmitted power by $t(\lambda) = |\tau(\lambda)|^2$

3. Computational simulation

Fig. 4 shows the steps of the algorithm. First, one is concerned with the input of the FBG-AOM dimensions, such as the radius and the length of the silica horn, the length of the taper and the length of the Bragg grating. In the second step the Finite Element Method is used to model the device, whereby a desired load is applied to the base of the silica horn. The result is the strain field calculated along the structure. However, only the strain field in the FBG region is used as the input to the transfer matrix method. The shift of the design wavelength along the z-axis as a function of the strain field is assumed as

$$\lambda_D(z) = \lambda_{D0} + (1 + (1 - p_e)\varepsilon(z)), \tag{27}$$

where p_e is the photoelastic coefficient and $\varepsilon(z)$ is the strain field calculated in the previous step through Eq. (11). It is important to note that this equation establishes the connection between the two methods. Finally, in the fourth step the TMM method gives the reflected and transmitted FBG spectra.

The structure is designed using 16,000 nodes/m. Each point along the structure corresponds to one element node. The dimensions of the structure employed in the calculation are shown in Fig. 5 and are taken from [10].

The quantity of nodes in the FBG region depends on its length. For example, for L = 5 cm, there are 800 elements in the grating region, which is enough to obtain an accurate strain field for frequencies up to 5 MHz. For higher frequencies the number of nodes per meter must be increased. The number of sections in the TMM is chosen to be the same as the number of elements used in the FEM for the grating region.

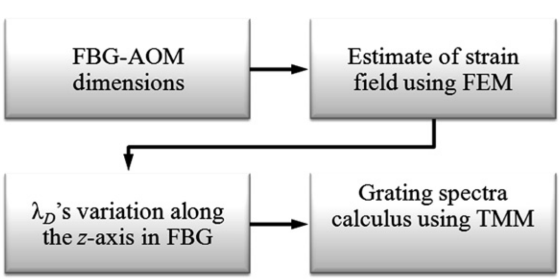

Fig. 4. Block diagram of the FBG-AOM simulation.

4. Results and discussion

Fig. 6a details the dimensions of the FBG-AOM used in the FEM model. The total structure size is 0.164 m, whereby the Silica horn is 0.07 m long. The taper diameter varies from 125 μm to 100 μm in 0.012 m and the FBG is 0.05 m long. Fig. 6b shows the resulting strain field along the structure length, calculated with the FEM. In the example, the discrete structure is excited with a 1 MHz acoustic wave of load amplitudes P_0 = 1.5 N and P_{DC} = 0 N, respectively. Particularly, the strain field in the grating is observed between the nodes located at 0.092 m and 0.142 m, as shown by the vertical dashed lines in Fig. 6a.

The behavior of the structure can be studied under the influence of parameters such as the frequency of the acoustical wave, the applied load or its dimensions. Using the dimensions given in Fig. 5 the following sections detail the behavior of the reflected grating spectrum as these parameters are varied.

4.1. Frequency variation

Fig. 7 shows the grating spectra calculated using the transfer matrix method. Fig. 7a shows the grating spectrum when no acoustical wave is applied. By exciting the structure with acoustical waves of different frequencies the grating spectrum is split showing other characteristic wavelengths. For the case shown in the figure the preload P_{DC} is chosen to be null and the amplitude of the

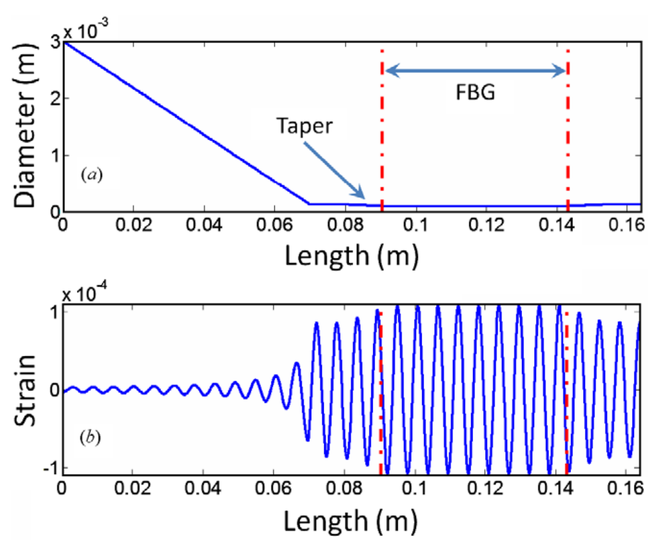

Fig. 6. (a) Diameter of the BG-AOM as function of the length. (b) Strain field along the FBG-AOM when is excited by a 1 MHz acoustic wave with P_0 = 1.5 N.

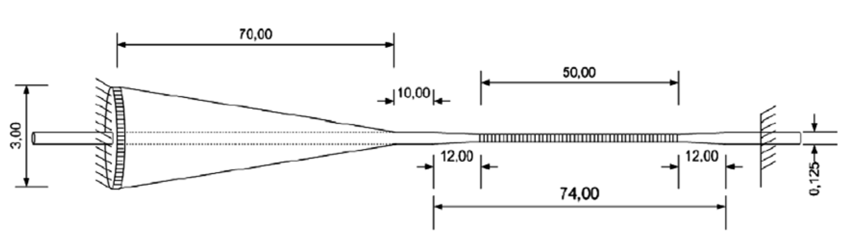

Fig. 5. Dimensions of FBG-AOM.

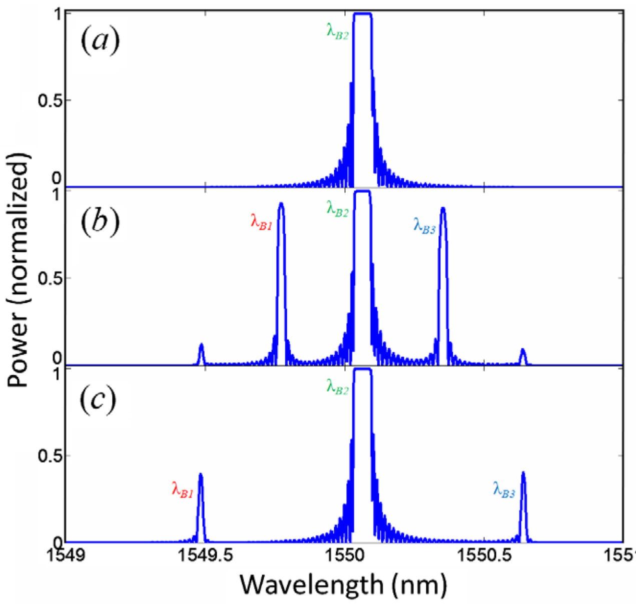

Fig. 7. FBG reflected spectrum when a 1.5 N fixed load and no pre-load ($P_{DC} = 0$) excitations are applied with (a) no acoustic wave, (b) frequency at 2 MHz and (c) 4 MHz.

harmonic load is chosen as $P_0 = 1.5$ N. This corresponds to the situation where the PZT actuator works in the stretching and compression regime, with symmetric displacement amplitude as seen in Fig. 7b.

At 2 MHz (Fig. 7b), simulation results show peaks at $\lambda_{B1} = 1549.77$ nm, $\lambda_{B2} = 1550.10$ nm and $\lambda_{B3} = 1550.35$ nm. The spectrum broadening is estimated as $\Delta\lambda = \lambda_{B3} - \lambda_{B1} = 0.58$ nm. As the acoustic frequency rises the side peaks get further apart (see Fig. 7c), but with lower reflectivity. At 4 MHz, $\Delta\lambda = 1.16$ nm. Note that the center wavelength $\lambda_{B2} = 1550.10$ nm remains stationary. Fig. 8 shows the linear behavior of the acoustic frequency versus $\Delta\lambda$, where the circles are experimental data retrieved from [21]. The graphic shows the main correlation between the experimental data and the theoretical result obtained with the present method.

4.2. Load variation

The load is related with the voltage applied to the PZT actuator. Keeping the frequency fixed at 1 MHz, the preload P_{DC} and the amplitude of the sinusoidal load P_0 are changed. Only the situation where positive voltage is supplied to the PZT actuator is considered. This can easily be achieved by setting an offset voltage in the RF generator.

Fig. 9a shows the reflected spectrum when P_0 and P_{DC} is 2.5 N and 0 N, respectively. Comparing with the previous case (see Fig. 7a and b) more side bands appear, however the central wavelength remains stationary. When the constant component P_{DC} is also set equal to 2.5 N the spectrum presents the same bands shown in Fig. 9a, however, it is shifted laterally in relation to the central band (see dashed line) in Fig. 9b. This is a consequence of the positive load generated by the PZT actuator, which causes a negative strain in the structure.

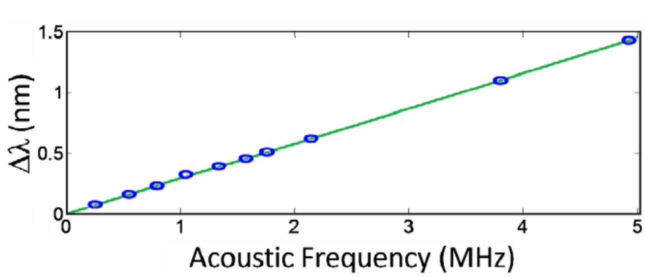

Fig. 8. Acoustic frequency versus spectrum broadening $\Delta\lambda$. The circles represent experimental results from [21].

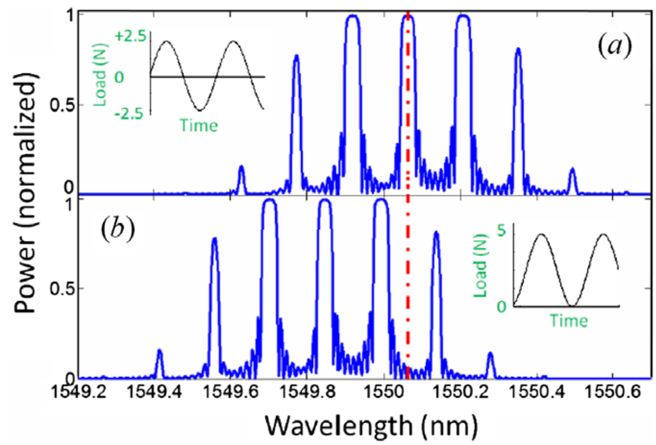

Fig. 9. FBG reflected spectrum when a 1 MHz acoustical excitation is applied with (a) $P_0 = 2.5$ N and $P_{DC} = 0$ N, (b) $P_0 = P_{DC} = 2.5$ N. The maximum FBG strain is $\varepsilon = 1.7924 \times 10^{-4}$ in case (a) and must as double for case (b).

If the P_0 and P_{DC} are set to a higher value, such as 4 N and 0 N, respectively, more side bands appear but the central band is strongly attenuated, as seen in Fig. 10a. The situation for $P_0 = P_{DC} = 4$ N is shown in Fig. 10b, where the lateral shift is larger as compared to the case in Fig. 9b. If the device could be put to work in the stretching regime the behavior would be the same, but the spectrum would shift to the higher wavelength region, as a result of a positive strain in the structure.

Preliminary results of this behavior are described in [23,24].

Most PZT actuators supply low loads as a result of the applied voltage. If high push loads (i.e., high compression stress) are used, buckling of the structure occurs and additional apparatus must be added to the system in order to avoid it. For example, in [25] supporting blades are used to avoid buckling of the grating.

4.3. Influence of the dimensions

One of the advantages of the present methodology is to assert the influence of the horn dimensions and the varying diameter of

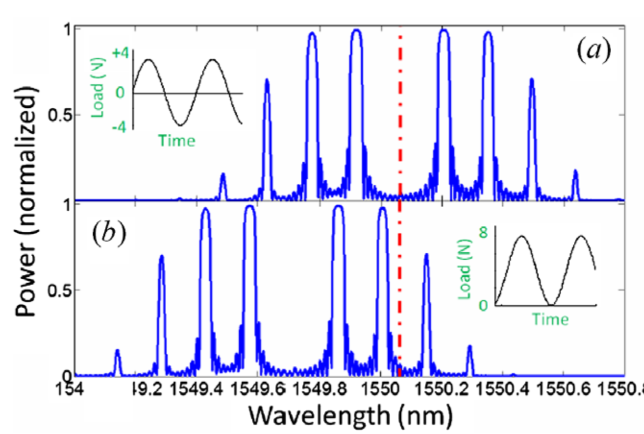

Fig. 10. FBG reflected spectrum when a 1 MHz acoustical excitations is applied with (a) $P_0 = 4$ N and $P_{DC} = 0$ N, (b) $P_0 = P_{DC} = 4$ N. The maximum FBG strain is $\varepsilon = 2.8678 \times 10^{-4}$ for the case (a).

the taper on the strain observed along the structure, allowing for the optimization of each one of its parts. Applying a constant load of $P_0 = 1$ N ($P_{DC} = 0$ N) and keeping the total length of the structure fixed at 0.164 m, changes in the dimensions of the silica horn and taper region modify the strain field seen by the grating. Fig. 11 shows the strain behavior as a function of the diameter (lower horizontal axis) and of the length (upper horizontal axis) of the silica horn. A modification of the horn dimensions causes changes in the device resonance frequencies. Numerical results show that an increase of the silica horn base diameter causes an increase in the stiffness and mass of the system, making the displacement and strain fields decrease along the FBG. On the other hand, a change of the silica horn length does not cause significant variations in these fields, as shown in Fig. 11. For a given device dimension the strain also varies with the PZT excitation frequency. Fig. 12 shows this behavior for the dimensions detailed in Fig. 5. One notes that the strain is higher for certain operation frequency that coincides with the resonance frequencies of the device. The FBG diameter can also be modified and, consequently, the taper region. In practice, this can be achieved by etching the fiber cladding till the desired diameter is reached. The taper is needed to enhance the acousto-optic interaction. Fig. 13 shows the variation of the maximum strain as a function of the fiber diameter in the grating region. The relationship between the taper and the maximum strain is also exponential.

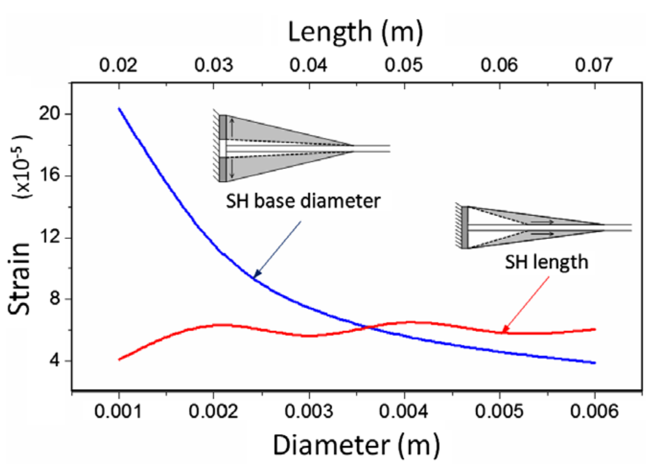

Fig. 11. Strain behavior versus the silica horn diameter and length.

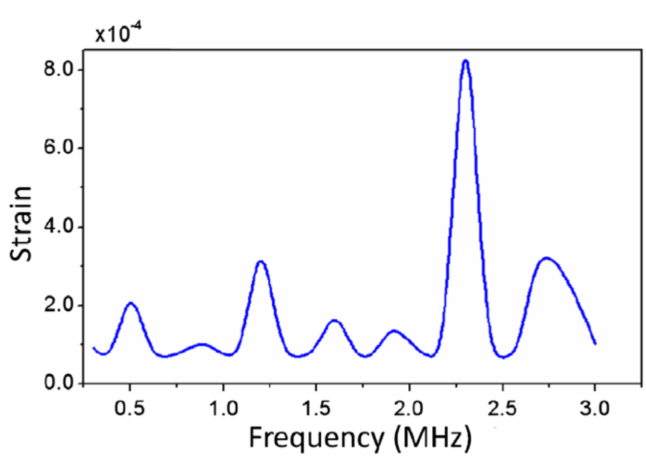

Fig. 12. Strain variation versus the PZT excitation frequency.

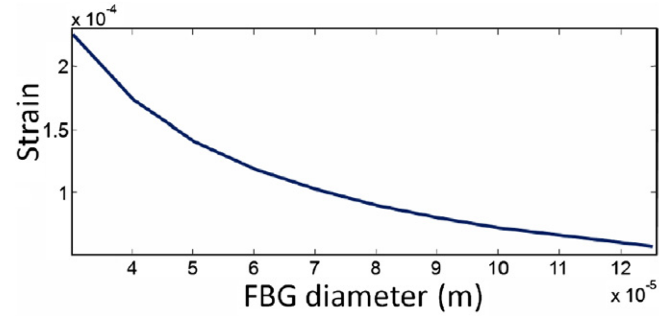

Fig. 13. Maximum strain in the grating as a function of its diameter. The taper increases the strain exponentially.

If the FBG length is modified, the acousto-optic interaction length will change. This results in the peak reflectivity change of the secondary lobules, λ_{B1} and λ_{B2}. For instance, Fig. 14 shows the relationship between the reflectivity of λ_{B1} and the FBG length.

Given an applied load, a set of similar curves can be used to optimize the design of the BG-AOM. Therefore, the strain can be adjusted according to adequate changes of the structure dimensions. For example, for a strain of $\varepsilon = 1.7924 \times 10^{-4}$ at 1 MHz, setting $P_0 = 2.5$ N (with the silica horn dimensions at 3 mm and 70 mm in diameter and length, respectively) gives the same results

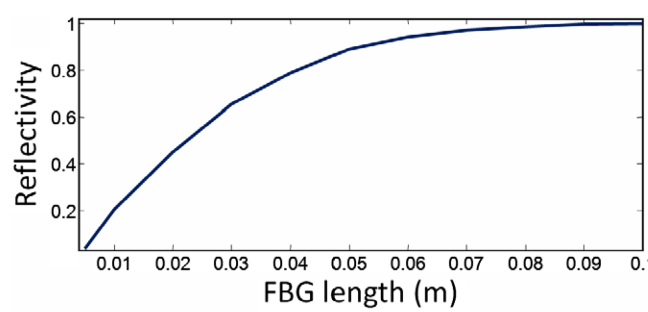

Fig. 14. Peak reflectivity of λ_{B1} as function of the FBG length.

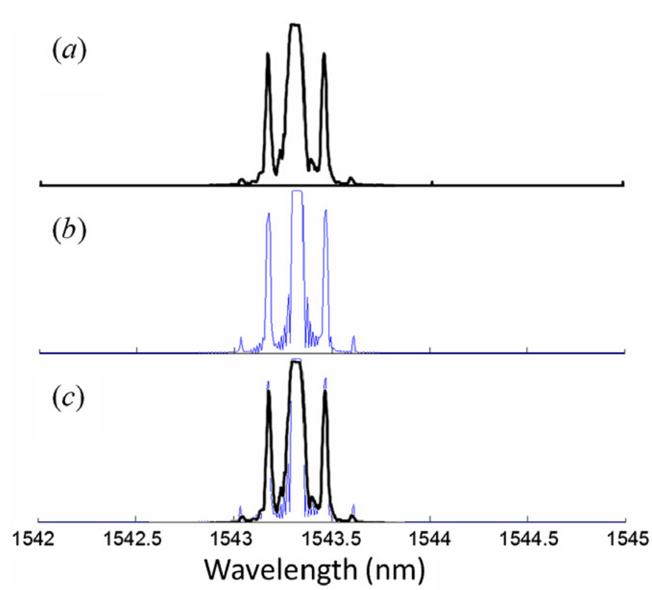

Fig. 15. Comparison of (a) the experimentally obtained spectrum from [21], (b) with the simulated for the structure excited with a 1 MHz acoustic wave at $P_0 = 1$ N. (c) Superposition of both (a) and (b) spectra.

as if designing the silica horn with 2 mm diameter and 70 mm in length for $P_0 = 1.714$ N, reducing the need for a higher applied load.

It also important to note that the taper itself does not modify the behavior concerning the separation between the side and the central peaks, as seen in Fig. 7, but only increase or decrease their reflectivity, i.e., the results shown in Fig. 8 are still the same with or without the taper.

The accuracy of the method can be verified by comparing the simulation with the experimental data available in the literature, such as the data obtained by Delgado-Pinar et al. [21]. Taking the dimensions of the structure presented by those authors, Fig. 15a shows the experimentally obtained spectrum by exciting the structure with a 1 MHz acoustic wave. Fig. 15b shows the simulated spectrum calculated using the two methods. As the strain value was not available in [21], simulations were performed with varying applied loads in order to fit the spectrum obtained experimentally. The best result was achieved with an applied load of $P_0 = 1$ N. Fig. 15c shows the superposition of both spectra. One observes that the spectra overlap very well concerning the central and the side peaks. The discrepancy in the side peaks reflectivity as compared to the same ones of the experimental result still reveals that the taper dimension needs to be adjusted.

5. Conclusions

The methodology presented here allows the design of a FBG-AOM, considering all components of the photonic structure (horn, taper and grating). The finite element and the transfer matrix methods present the advantage of asserting the strain along the whole structure making it possible to determine the influence of the structure dimensions (horn, taper and FBG sizes) on the grating reflected spectrum for an acoustical wave propagating along its axis. Furthermore, the physical characteristics of the structure can be adjusted in order to obtain the desired strain and spectrum. The approach takes into account the load induced by the acoustical wave, which can be associated with the characteristics of the PZT actuator used for its excitation (for example, the maximum pull and/or push load and maximum displacement delivered by the actuator).

The simulation results obtained using the method correlate well with experimental data in similar structures presenting the same dimensions [6,20,21], which demonstrates that the method is very accurate to solve the problem.

Acknowledgements

R.A. Oliveira and P.T. Neves Jr. thanks the support of Coordenação de Aperfeiçoamento de Pessoal de Ensino Superior (CAPES) by means of a research scholarship.

References

[1] B.Y. Kim, J.N. Blake, H.E. Engan, H.J. Shaw, Opt. Lett. 11 (6) (1986) 389.
[2] T.A. Birks, P.St.J. Russel, D.O. Culverhouse, J. Lightwave Technol. 14 (11) (1996) 2519.
[3] R. Feced, C. Alegria, M.N. Zervas, R.I. Laming, IEEE J. Selected Top. Quant. Electron. 5 (5) (1999) 1278.
[4] A. Díez, M. Delgado-Pinar, J. Mora, J.L. Cruz, M.V. Andrés, IEEE Photon. Technol. Lett. 15 (1) (2003) 84.
[5] H.F. Taylor, J. Lightwave Technol. LT-5 (1987) 990.
[6] W.F. Liu, P.St.J. Russell, L. Dong, Opt. Lett. 22 (19) (1997) 1515.
[7] W.F. Liu, I.M. Liu, L.W. Chung, Opt. Lett. 25 (18) (2000) 1319.
[8] P. Russell St., Phys. Rev. Lett. 56 (6) (1986) 596.
[9] D.-W. Huang, W.-F. Liu, C.-W. Wu, C.C. Yang, IEEE Photon. Technol. Lett. 12 (2) (2000) 176. February.
[10] M. Delgado-Pinar, A. Díez, J.L. Cruz, M.V. Andrés, Appl. Phys. Lett. 90 (2007) 171110.
[11] R.N. Thurston, J. Acoust. Soc. Am. 64 (1) (1978) 1.
[12] O.C. Zienkiewicz, R.L. Taylor, The Finite Element Method, vol. 1, The Basis, Oxford, Butterworth-Heinemann, 2000.
[13] T.J.R. Hughes, The Finite Element Method – Linear Static and Dynamic Finite Element Analysis, Prentice-Hall, Englewood Cliffs, NJ, 1987.
[14] M. Prabhugoud, K. Peters, Smart Mat. Struct. 15 (2006) 550.
[15] H. Kogelnik, in: T. Tamir (Ed.), Theory of Optical Waveguides, in Guided-Wave Optoelectronics, Springer-Verlag, New York, 1990.
[16] K.O. Hill, G. Meltz, J. Lightwave Technol. 15 (8) (1997) 1263.
[17] T. Erdogan, J. Lightwave Technol. 15 (8) (1997) 1277.
[18] R. Kashyap, Fiber Bragg Gratings, Academic Press, San Diego, 1999.
[19] W.F. Liu, Philip St. J. Russell, L. Dong, J. Lightwave Technol. 16 (11) (1998) 2006.
[20] M. Delgado-Pinar, J. Mora, A. Díez, J.L. Cruz, M.V. Andrés, IEEE Photon. Technol. Lett. 17 (3) (2005) 552.
[21] M. Delgado-Pinar, D. Zalvidea, A. Díez, P. Pérez-Millán, M.V. Andrés, Opt. Express 14 (3) (2006) 1106.
[22] W.P. Mason, J. Acoust. Soc. Am. 28 (6) (1956) 1197.
[23] R.A. Oliveira, P.T. Neves Jr., A.A.P. Pohl, J.T. Pereira, in: Proceedings of CLEO Pacific Rim, 2007, p. 820.
[24] R.A. Oliveira, P.T. Neves Jr, A.A.P. Pohl, J.T. Pereira, in: Proceedings of IMOC 2007, Research Publishing Services, Chennai, 2007, p. 716.
[25] N. Mohammad, W. Szyszkowski, W.J. Zhang, E.I. Haddad, J. Zou, W. Jamroz, R. Kruzelecky, J. Lightwave Technol. 22 (8) (2004) 2001.